




# Epitaxial pyrolytic carbon coatings templated with defective carbon nanotube cores for structural annealing and tensile property improvement

Fan Liu<sup>1,\*</sup> , Keiichi Shirasu<sup>2</sup>, and Toshiyuki Hashida<sup>1</sup>

<sup>1</sup> Fracture and Reliability Research Institute, Tohoku University, 6-6-11, Aza-Aoba, Aramaki, Aobaku, Sendai, Miyagi 980-8579, Japan

<sup>2</sup> Department of Aerospace Engineering, Tohoku University, 6-6-01, Aza-Aoba, Aramaki, Aobaku, Sendai, Miyagi 980-8579, Japan

Received: 5 April 2021

Accepted: 10 September 2021

Published online:  
17 September 2021

© The Author(s), under exclusive licence to Springer Science+Business Media, LLC, part of Springer Nature 2021

## ABSTRACT

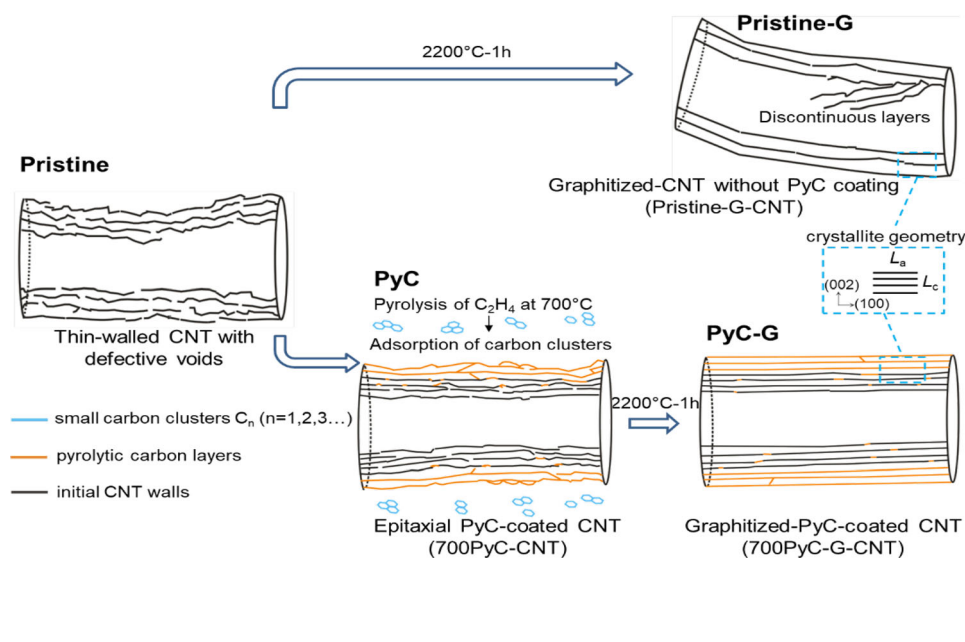
Thermal annealing of chemical vapor deposition (CVD)-grown carbon nanotubes (CNTs) is a practical method for reducing defects in CNTs, which is essential for promoting applications of CNTs in nanoscale or microscale materials. However, the increase in annealing temperature fails to bring noticeable improvements in the tensile properties of CNTs, implying the negative influence of carbon sublimation on the defect healing process. Here we propose a two-step annealing strategy for improving the microstructure and tensile properties of CVD-grown CNTs. This has been achieved through the epitaxial growth of pyrolytic carbon thin layers at the CNT surface and then followed by graphitization treatment at 2200 °C for 1 h. Tensile performances of two-step annealed CNTs have been investigated by in situ tests in a scanning electron microscope. The results show that the average Young's modulus and fracture strength of two-step annealed CNTs are improved approximately by 35% and 10%, respectively, compared to those of one-step annealed CNTs. Such an enhancement can be ascribed to the well-aligned CNT walls with fewer structural defects, supported by the characterization results from transmission electron microscope, X-ray diffraction and Raman spectroscopy. The two-step annealing strategy developed in this study for improving the mechanical properties of CNTs is expected to be applicable to a practical fabrication process.

Handling Editor: Yaroslava Yingling.

Address correspondence to E-mail: fan.liu@rift.mech.tohoku.ac.jp

<https://doi.org/10.1007/s10853-021-06523-8>

## GRAPHICAL ABSTRACT



## Introduction

Carbon nanotubes (CNTs) are predicted to have unparalleled tensile strength (100 GPa) and Young's modulus (1 TPa) due to the strong cohesive force of C–C covalent bonds [1]. In the past two decades, chemical vapor deposition (CVD)-grown CNT arrays have attracted great attention due to their unique spinnability [2, 3] and large yields [4]. However, there is a common understanding that the quality of CVD-grown CNTs is inferior to that of arc discharge (AD)-grown CNTs because the former usually has a higher degree of disorder compared to the latter [5]. CNT strength may significantly decrease by 26–50% due to the influence of defects, supported by experiments and simulation studies [6, 7]. Thus, a cost-effective method to remove the inherent defects in CVD-grown CNTs is always being sought after in order to improve the mechanical properties of CNTs.

To produce nanotubes with fewer defects, some important reasons for the annealing of CVD-grown CNTs are reviewed below. The typical CVD synthesis temperature is lower than  $1000^\circ C$  [8], obviously different from that of arc discharge growth ( $\sim 3000^\circ C$ ). Naturally, furnace annealing of CVD-grown

CNTs at graphitization temperatures ( $> 2150^\circ C$ ) has been suggested as the prevalent method for defect healing. Meanwhile, annealing can remove catalyst particles and convert carbonaceous impurities into highly crystalline materials, which may decrease the possibility of introducing additional defects in the CNT microstructure compared to other purification methods (e.g., sonication, selective oxidation, acid etching) [9].

However, there is still a lack of understanding of the microstructure–tensile property relationship of annealed CVD-grown CNTs. Shirasu et al. [10] evaluated the tensile properties of CNTs (outer diameter  $\sim 40$  nm) that were thermally annealed at  $2900^\circ C$ , but the results showed only a minor improvement compared to those of Pristine-CNTs. Therefore, if thermal energy is the only dominating factor for defect healing, why does the tensile strength of CVD-grown CNTs annealed at extremely high temperatures not significantly improve to approach the strength of AD-grown CNTs? Previous studies reported that some gross defects, e.g., sharp kinks [11], chasm-like voids [12, 13], discontinuous flaws [14] might remain even after annealing at  $3000^\circ C$ , which may explain the absence of noticeable

improvements in tensile properties. Besides, during the annealing of thin-walled CNTs (outer diameter  $\leq 25$  nm), some special phenomena have been reported: (1) In situ TEM joule heating experiment observed the peeling of CNT outer walls at over 2000 °C [15]; (2) ex situ experiments showed that some inner tubes of multi-walled CNTs disappeared or collapsed after annealing [16, 17], forming a large hollow core. The above clues imply one factor that we may have neglected—sublimation of carbon atoms at the temperature that is close to or even higher than the premelting point of defective CNTs ( $\sim 2300$  °C [18]). Therefore, the structural evolution of thin-walled CNTs is possibly sensitive to the carbon sublimation during the graphitization process, which inevitably influences the defect healing effect and the resulting mechanical strength.

Inspired by the above idea, we suggest a two-step annealing strategy for improving the quality of CVD-grown CNTs. First, we deposit epitaxial pyrolytic carbon (PyC) layers onto the surfaces of defective CNTs to supply carbon sources. The second step is to anneal PyC-coated CNTs at graphitization temperatures. Given enough thermal energy, epitaxial PyC deposits may be “digested” to compensate for the carbon sublimation; meanwhile, the migration of pyrolytic carbon atoms can facilitate the structural annealing of CNTs. We have conducted a comprehensive material characterization (TEM, XRD, Raman) and in situ SEM tensile tests for CNTs. We have discussed the fitting between the fracture strength (Young’s modulus) and the in-plane crystallite size calculated from the Raman D/G intensity ratio, to reveal the microstructure–tensile property relationship of annealed CVD-grown CNTs. To the best of our knowledge, only few groups [19–21] are focusing on the experimental tensile properties of CVD-grown CNTs compared to the extensive studies [22–27] of AD-grown CNTs. We demonstrate the usefulness of the two-step annealing method to improve the crystallinity and mechanical properties of CNTs, on the basis of the structural parameters evaluated by the various characterization techniques.

## Experimental procedure

CVD-grown thin-walled carbon nanotube sheets (LINTEC OF AMERICA, INC., Nano-Science & Technology Center) were used as a Pristine-CNT

sample in this study. The outer diameter of CNTs is  $\sim 10$  nm, and the size of the CNT sheets is approximately  $50 \text{ mm} \times 20 \text{ mm} \times 10 \text{ }\mu\text{m}$  with 50 stacking layers. To deposit pyrolytic carbon (PyC) onto CNT surfaces, the CNT sheets were placed in a quartz tube reactor for the pyrolysis of ethylene ( $\text{C}_2\text{H}_4$ ). The furnace temperature was heated to 700 °C in 20 min in vacuum, then  $\text{C}_2\text{H}_4$  (100 sccm) and argon (400 sccm) were introduced, and the total pressure in the reactor chamber was kept at 2.5 kPa for 30 min. After pyrolysis, the reactor was purged with flowing argon (800 sccm) and cooled down to room temperature. Because of the highly porous nature of CNT sheets drawn from arrays, the spacing between intertube voids was reported to be hundreds of nanometers [28]. Thus, the penetration of ethylene molecules inside the CNT sheets during the pyrolysis is considered to be sufficient for the carbon supply.

PyC-coated CNT sheets were subjected to further heating in an electric resistance furnace (Thermocera, TCF-C500) for graphitization treatment. The following heating steps were applied: 20 °C/min from room temperature to 1400 °C, 10 °C/min from 1400 to 2200 °C, keeping 2200 °C for 60 min and then cooling down. The whole process was conducted under highly pure (99.9999%) argon flowing at the rate of 1000 sccm. The CNT sheets were annealed within the isothermal zone of the furnace ( $70 \text{ mm} \times 70 \text{ mm} \times 100 \text{ mm}$ ). As a control group, the graphitization of Pristine-CNT sheets was conducted under argon atmosphere using the identical heating steps. The masses of CNT sheet samples were measured with an analytical balance (A&D, BM-252) with readability to 0.01 mg.

XRD was performed using an X-ray diffractometer (Rigaku, SmartLab) with a Cu  $K\alpha$  target ( $\lambda = 0.154 \text{ nm}$ ), and the continuous scan ( $0.5^\circ/\text{min}$ ) was conducted in the range between 15 and  $50^\circ$ . Raman spectra were obtained by a spectrometer (Chromex, Inc250) with the laser excitation wavelength of 532 nm. Raman measurements ( $50 \times$  magnification) were carried out under ambient conditions, and at least 9 points were measured in different locations across each CNT sample.

TEM samples were prepared by dispersing a small amount of CNTs in ethanol solution, and then, sonication lasted only for 1 min to avoid possible damages. A droplet of dispersed nanotubes was deposited on a copper TEM grid, and CNT morphology was observed using TEM (JEOL, JEM-2100)

under 200 kV at an exposure time of less than 1.5 s. To calculate the average diameter of each sample, nearly 100 measurements were taken from high-magnification (1500 k $\times$ ) TEM pictures using an image processing software (ImageJ). We also performed a fast Fourier transformation (FFT) analysis along the nanotube axis using high-magnification (1500 k $\times$ ) TEM images to obtain electron diffraction patterns. Based on the azimuthal intensity variation analysis [29], at least 50 random CNT segments from each sample were analyzed to calculate the average misalignment angle of CNT walls relative to the tube axis.

In situ tensile tests of individual CNTs were conducted with a nanomanipulator inside the SEM chamber (JEOL, JSM-6510). During the tests, a cantilever connected with one nanotube moved upward to initiate the tension until the failure. The principle of the tensile method was firstly reported by Yu et al. [26], and our previous work has summarized the details of the test procedures employed in this study [30]. In brief, atomic force microscopes (AFM of PPP-NCL, force constant of 4.4–5.2 N/m; and AFM of PPP-CONTR, force constant of 0.18–0.44 N/m) served as force sensors. An individual CNT was clamped onto the cantilever tip by electron beam-induced deposition of carbonaceous materials. The tension force applied to the nanotube was calculated from the deflection of the cantilever tip, and the tube elongation was determined by counting the pixel number in acquired SEM videos. After the tensile tests, CNT fragments would remain on the cantilever tip, which was later transferred to the TEM sample stage (Hitachi, HF-2000) to observe the fracture morphology. The fractured cross-sectional area for each broken CNT was calculated from the precisely measured tube diameter instead of the average tube diameter from a group of CNTs.

## Results and discussion

The Pristine-CNT samples used in this study show irregular lattice fringes with defective voids (marked by red circles in Fig. 1a), indicating their low crystallinity. To obtain the best morphology of epitaxial PyC layers at the CNT surface, we conducted a series of ethylene (C<sub>2</sub>H<sub>4</sub>) pyrolysis treatment of Pristine-CNTs at 700 °C, 800 °C, 900 °C, 1000 °C, respectively (keeping ethylene partial pressure and treatment

time identical). The morphologies of PyC-coated CNTs at different pyrolysis temperatures are shown in Fig. S1. When the pyrolysis temperature increases, PyC-coated CNTs evidently become thicker. However, the disorder degree of deposited PyC layers seems to increase with the pyrolysis temperature. Thus, we choose to obtain epitaxial PyC-coated CNTs via C<sub>2</sub>H<sub>4</sub> pyrolysis at 700 °C under the partial pressure of 500 Pa for 30 min, named as 700PyC-CNTs hereinafter. For 700PyC-CNTs, it is difficult to distinguish new carbon layers from the initial CNT walls except for some wrinkled graphene flakes (marked by the white arrows in Fig. 1b). The growth mechanism of thin PyC layers in this study may be different from the report by Monthieux et al. [31], in which hydrocarbon droplets are formed in the bulk gas phase and then depositing onto CNTs under high temperatures (1100–1295 °C) and high pressures (~ 100 kPa). Presumably the growth of thin PyC layers might initiate with the adsorption of small carbon clusters onto the active sites (e.g., vacancies) of CNT surfaces, which is partially similar to the formation of lateral carbon deposits reported by Kuznestov et al. [32]. The growth kinetics under our pyrolysis conditions (low-temperature and low-pressure) will be described in our companion paper to discuss the effect of active sites on the PyC deposition at the CNT surface. Most importantly, epitaxial PyC thin layers with a rough laminar structure (partially aligned graphene flakes along the nanotube length) can serve as the foundation of “graphitizable” PyC-coated CNTs.

Graphitization of Pristine-CNTs was conducted at 2200 °C for 1 h, named as Pristine-G-CNTs hereinafter. Pristine-G-CNTs exhibit a clean surface (Fig. 1c), but some sharply kinked walls may still exist (marked by yellow dashes). The typical morphology of discontinuous flaws at the inner walls is shown in Fig. S2. This observation is in line with the previous literature that reported the formation of discontinuous inner layers in annealed CNTs [33]. In contrast, highly crystalline nanotubes with straight lattice fringes (Fig. 1d) were obtained by graphitization of 700PyC-CNTs at 2200 °C for 1 h (named as 700PyC-G-CNTs hereinafter). Marked by the white arrow in Fig. 1d, the closed cap at the tube end shows a high stacking order.

A common approach to characterize the crystallite dimensions of CNTs is the X-ray diffraction. The spectra in Fig. 2a show (002) peaks at 26.00–26.40°

**Figure 1** TEM images of CNT samples at different treatment stages: Pristine-CNTs (a); PyC-coated CNTs via C<sub>2</sub>H<sub>4</sub> pyrolysis at 700 °C–500 Pa–30 min (b), the magnified inset in (b) shows the deposited graphene flakes; Pristine-CNTs after graphitization (c); 700PyC-CNTs after graphitization (d). The histogram distribution of CNT diameters is shown in Fig. S3.

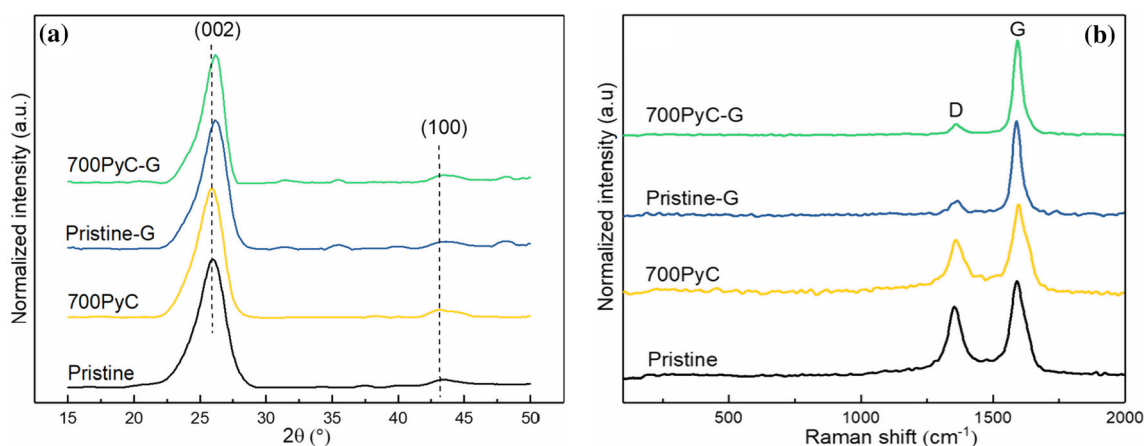
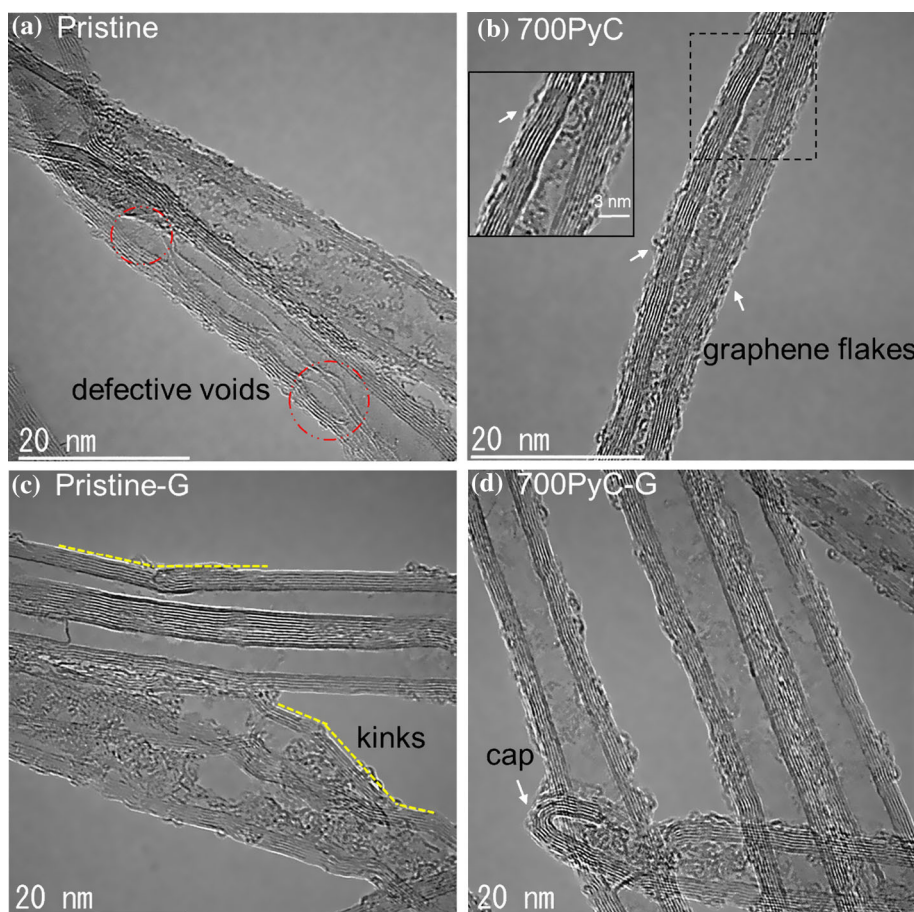


**Figure 2** XRD patterns (a) and Raman spectra (b) of Pristine- and 700PyC-CNTs before and after graphitization at 2200 °C for 1 h.

and broad (100) peaks at 42.90–43.20°. The average crystallite thickness ( $L_c$ ) or crystallite size ( $L_a$ ) can be calculated from the full width at half-height of (002) or (100) peaks, respectively [34]. The (002) peak of annealed nanotubes (Pristine-G- and 700PyC-G-CNTs) shifts to higher angles compared to that of

pristine ones, leading to a decrease in the interlayer spacing  $d_{002}$  [35]. In contrast, we note that the  $d_{002}$  of 700PyC-CNTs is significantly increased to 3.43 Å (listed in Table 1), probably indicating the turbostratic propensity of as-deposited pyrolytic carbon

**Table 1** Structural parameters of CNTs, including interlayer spacing ( $d_{002}$ ), crystallite thickness ( $L_c$ ), crystallite size ( $L_a$ ) by XRD; integrated intensity ratio ( $I_D/I_G$ ), full width at half-maximum of G-peak (G-FWHM), in-plane crystallite size ( $L_a^R$ ) through Cancado's equation [38] from Raman spectra; misalignment angle ( $\theta$ ) between CNT walls and the tube axis by FFT azimuthal scan of (002) diffraction arcs

CNT sample	XRD			Raman			FFT
	$d_{002}$ (Å)	$L_c$ (nm)	$L_a$ (nm)	$I_D/I_G$	G-FWHM ( $\text{cm}^{-1}$ )	$L_a^R$ (nm)	$\theta$ (°)
Pristine	3.40	2.90	4.16	0.85	58.92	23	16.43
Pristine-G	3.38	3.19	7.82	0.36	40.25	54	13.38
700PyC	3.43	3.14	7.73	0.75	59.57	26	16.20
700PyC-G	3.38	3.73	9.15	0.32	34.57	60	10.69

layers, which is compatible with the XRD results by Faraji et al. [36].

The first-order Raman spectroscopy was conducted for each CNT sample. G-peak ( $1580 \text{ cm}^{-1}$ ) originates from  $sp^2$  carbon networks while D-peak ( $1350 \text{ cm}^{-1}$ ) arises from structural defects; thus, the D/G intensity ratio can be applied as an indicator of defect density [37]. The normalized spectra (Fig. 2b) clearly show the difference in the D-peak height of 700PyC-G-CNTs compared to that of the other samples. By using Cancado's empirical equation of nanographite [38], we can roughly estimate the in-plane crystallite size in CNTs ( $L_a^R = 2.4 \times 10^{-10} \times \lambda_{\text{laser}}^4 \times \left(\frac{I_D}{I_G}\right)^{-1}$ ), where  $\lambda_{\text{laser}}$  is the wavelength of the laser source. From Table 1, the intensity ratio ( $I_D/I_G$ ) of 700PyC-G-CNTs is lower than that of Pristine-G-CNTs, leading to a larger  $L_a^R$  that is consistent with our XRD results. The full width at half-maximum of G-peak (G-FWHM) of 700PyC-G-CNTs is much smaller than that of the other samples, indicating that two-step annealed CNTs possess the highly graphitic microstructure. The mechanism will be discussed later. Besides, the  $I_D/I_G$  of 700PyC-CNTs has slightly decreased relative to that of Pristine-CNTs. Such a phenomenon that occurred in PyC-coated CNTs was rarely reported except Kuznetsov's research [39], which explained the decreased  $I_D/I_G$  as the result of dangling bond saturation at the open edge of graphene. Similarly, the adsorption of carbon clusters during the growth of thin PyC layers may fill in some vacancy sites at the CNT surface, inducing the decrease in  $I_D/I_G$ .

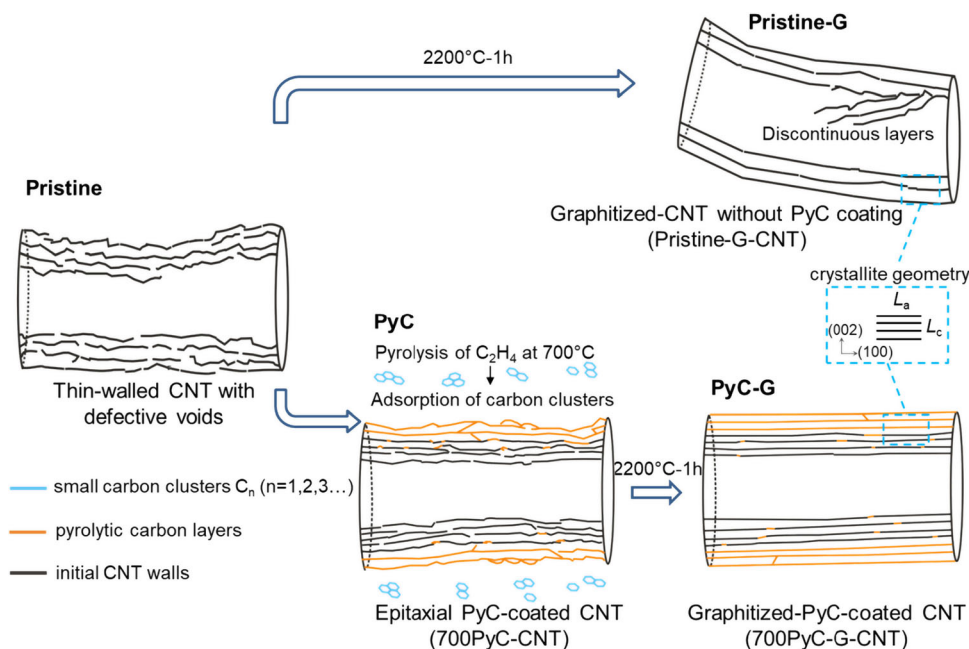
As a practical method to evaluate the straightness of CNT walls [40], a fast Fourier transform (FFT) analysis of individual CNTs was performed along the tube axis. Typical diffraction patterns of each sample

are given in Fig. S4, in which we notice sharp (002) spots or blurred (002) arcs due to the crystallinity difference. The azimuthal intensity variation is plotted and fitted with a Gaussian function (one example is shown in Fig. S5). One-half of the peak width at the half-height of the azimuthal peak ( $\frac{1}{2}$ FWHM) can indicate the misalignment angle  $\theta$  of CNT walls relative to the tube axis [41]. According to the last column in Table 1, the alignment of the graphitic layers in 700PyC-G-CNTs is better than that in Pristine- and Pristine-G-CNTs.

From the above characterization results, we suggest that the structural evolution of 700PyC-G-CNTs should differ from that of Pristine-G-CNTs, mainly revealed by larger crystallite sizes and a smaller misalignment angle between CNT walls and the tube axis. Therefore, Fig. 3 illustrates the possible differences in the graphitization mechanism between one-step annealed CNTs (Pristine-G) and two-step annealed CNTs (700PyC-G).

The previous study [12] indicated that annealing of CNTs could repair internal defects and the defect healing effect strongly improves with the increasing annealing temperature. But some gross defects (kinks, voids, discontinuous flaws) may be difficult to be removed even at extremely high temperatures ( $\sim 3000 \text{ }^\circ\text{C}$ ), which is probably resulted from the influence of carbon sublimation. In theory, the increasing heat energy of atomic lattices under graphitization temperatures ( $\geq 2150 \text{ }^\circ\text{C}$ ) brings significant thermal agitation and causes the sublimation of some carbon atoms from the original lattice for a more entropic benefit in the gas state. However, numerical simulations [42] have shown that the location of carbon loss is not random. If Pristine-CNTs with voids (vacancies) are annealed above 2150

**Figure 3** Illustration of the structural evolution during the graphitization process (2200 °C-1 h) of thin-walled defective CNTs without PyC coatings (Pristine-G) or with epitaxial PyC coatings (PyC-G).



°C, some carbon atoms may be sublimated through the lowest energy channel, which was reported to correlate with the shuttling or spiral movement of topological 5/7 pairs [43]. Note that the sublimation discussed in this paper refers to the ejection of carbon atoms from the defective graphene lattice. We infer that some of the sublimated carbon atoms may return and then diffuse to the energy favorable sites on CNT surfaces as a result of atomic collisions, but the rest of them may be carried away by the flowing argon. According to Huang et al. [44], the sublimation process can heal vacancies but tends to form kinks in CNT walls. The atoms around the kinked location may be heavily stressed because the graphene lattice is warped. Presumably the relief of internal stress generated by kinked walls might induce new types of structural defects such as interlayer detachment. Therefore, the detachment of innermost one or two graphene layers from the other layers may explain the discontinuous layers at the inner walls of Pristine-G-CNTs (as illustrated in Fig. 3).

Next, the structural evolution of two-step annealed CNTs (700PyC-G) is explained. During the first step (pyrolysis), small carbon clusters ( $C_n$ ) are one of the products from the decomposition of ethylene [45]. Then the growth of PyC layers initiates with the adsorption of carbon clusters onto the vacancy sites at the CNT surface, and the supplied carbon clusters may interact with vacancies to form adatom–vacancy pairs between adjacent graphene layers [46]. During

the second step (graphitization), the self-diffusion rate of carbon dramatically increases when the temperature rises above the Debye temperature of graphite (2000 K) [47]. The thermally induced motion of carbon atoms at the interface between CNT walls and PyC layers was reported [48] to decrease the activation energy for the phase transition from turbostratic carbon into graphitic carbon. Presumably the carbon atoms from the outer PyC coating may diffuse along the axial or radial direction of nanotubes, and such an atomic migration can promote their incorporation into the defective graphene lattice [49], leading to the reconstruction of CNT walls (as illustrated in Fig. 3). Distinct from the one-step annealing without carbon supplying, our two-step annealing strategy firstly masks the vacancies on CNT surfaces by the graphitizable PyC deposits, which can facilitate the defect healing at high temperatures [50]. To summarize, the structural evolution from 700PyC- to 700PyC-G-CNTs is a stepwise regrowth process of graphitic crystallites: (1) straightening the wrinkled graphene flakes; (2) healing discontinuous CNT walls assisted by the migration of pyrolytic carbon atoms; (3) increasing the crystallite dimensions and decreasing the misalignment angle between CNT walls and the tube axis.

For a measure of the carbon sublimation loss, we conducted a gravimetric examination of Pristine-, Pristine-G-, 700PyC-, 700PyC-G-CNT sheets (Table S1). The results show that the Pristine-G-CNT

sheet loses 3.6% of its mass compared to the pristine sheet. In comparison, the mass of the 700PyC-CNT sheet after the pyrolysis step has increased by 5.3% compared to that of the pristine sheet; after the graphitization step, the mass of the 700PyC-G-CNT sheet is still 1.3% higher than that of the pristine sheet, clearly demonstrating that the deposited PyC during the pyrolysis step can compensate the carbon sublimation loss at graphitization temperatures. During the graphitization of PyC-coated CNTs, we infer that some carbon atoms from the outer PyC layers may also be sublimated, but it can inhibit the carbon loss from the inner CNT walls.

Since 700PyC-G-CNTs exhibit the improved structural parameters (wall straightness and crystallite size) compared to Pristine-G-CNTs, then we examine the differences in the tensile properties between two-step annealed CNTs and one-step annealed CNTs. In situ tensile tests for the CNTs were conducted in SEM using AFM cantilevers and the nanomanipulator. Here we compared the currently available data from 35 individual nanotubes (Pristine, Pristine-G, 700PyC, 700PyC-G). Tensile results for each fractured nanotube are summarized in Table 2, including outer and inner diameter, breaking forces, failure strains, etc. The fracture strength of CNTs is calculated by dividing the breaking force by the cross-sectional area of all the broken walls, full details of the calculation method can be found in our previous review [30].

The average values and standard deviations of the fracture strength and Young's modulus are plotted in Fig. 4a. 700PyC-G- and Pristine-G-CNTs both exhibit a higher average value for Young's modulus and fracture strength relative to those of Pristine-CNTs. Notably, the Young's modulus of 700PyC-G-CNTs is significantly higher than that of Pristine-G-CNTs. With regard to the fracture strength, the lower bound of strength for 700PyC-G-CNTs is close to the average value of Pristine-CNTs. The fracture strength of 700PyC-CNTs seems to be lower than that of Pristine-CNTs. The possible explanation is that the turbostratic propensity of PyC deposits might induce the weak strength of the outermost PyC layer and then premature failure occurs [7].

Klein et al. [51] proposed that the two-parameter Weibull distribution can be applicable to the strength data of the CNTs with roughly similar surface areas ( $\pi DL$ ). The equation can be written as:  $\ln(-\ln[1 - P_f(\sigma)]) = \beta \ln(\sigma) - \beta \ln(\alpha)$ , where  $P_f(\sigma)$  is

the cumulative failure probability,  $\sigma$  is the fracture strength,  $\alpha$  and  $\beta$  are the Weibull scale parameter and shape parameter, respectively. (The complete derivation and analysis are given in Supplementary Information, Table S3.) Accordingly, we plot the Weibull distribution of the fracture strength from Pristine-, Pristine-G-, 700PyC-G-CNTs (Fig. 4b). Three fitted lines (regression coefficient  $\geq 0.86$ ) have captured the general trend of our strength data, in which the Weibull shape parameter can be obtained from the line slope. Pristine-CNTs exhibit a low shape parameter ( $\beta_P \sim 1.8$ ), suggesting a large variability in tensile strength. In contrast, the larger shape parameters for 700PyC-G ( $\beta_{C-G} \sim 3.1$ ) and Pristine-G ( $\beta_{P-G} \sim 2.9$ ) indicate their reduced strength scattering, which can be ascribed to the decreased defect density after graphitization. Thus, 700PyC-G-CNTs exhibit the improved strength reliability compared to Pristine-CNTs. Gao et al. reported [52] that the large variability in CNT strength may have a strongly negative effect on the mean strength of CNT yarns because of the irregularly distributed load sharing between each nanotube.

Typical SEM and TEM images of CNTs before and after tensile testing are collected. The typical fracture behavior for Pristine-G samples is the "sword-in-sheath" (Fig. 5a, b), while Pristine- and 700PyC-CNTs usually fail in the "clean break" (Fig. S6a–c). The prevalent fracture behavior of 700PyC-G is close to that of Pristine-G (Fig. 5c, d) because the sword part of CNT fragments can be observed in the inset of Fig. 5d. However, we also notice one special case of 700PyC-G (Fig. 5e, f): its sword part after failure is absent in SEM images, and the "clean break" is confirmed by TEM (inset of Fig. 5f). We found only two samples with the "clean break" among 10 tested 700PyC-G-CNTs. The different fracture behaviors of nanotubes can be explained by the cross-linking level (interwall  $sp^3$  bonds) between CNT walls [53]. For Pristine-CNTs with vacancies, dangling bonds around the vacancy edge might induce the interwall bonding, which is beneficial to the load transfer and the "clean break" fracture [54]. For Pristine-G-CNTs, the graphitization process promotes the microstructural reorganization and eliminates vacancies; meanwhile, it may be accompanied by the reduction of interwall bonds in CNTs, causing the "sword-in-sheath" fracture [20]. For 700PyC-G-CNTs, the pyrolysis step induces the adsorption of carbon clusters onto defective CNT surfaces (adatom-



**Table 2** Tensile data of individual CNT samples. Values shown are outer and inner diameters ( $D$  and  $d$ ), gauge length ( $L$ ), breaking force ( $F_b$ ), Young’s modulus ( $E_f$ ), fracture strength ( $\sigma$ ), failure strain ( $\epsilon$ ). The statistical analysis of  $E_f$  and  $\sigma$  with the 95% confidence level is offered in Supplementary Information (Table S2)

Type	No	$D, d$ (nm)	$L$ ( $\mu\text{m}$ )	$F_b$ (nN)	$E_f$ (GPa)	Mean $E_f$ (GPa)	$\sigma$ (GPa)	Mean $\sigma$ (GPa)	$\epsilon$ (%)
Pristine	P-1	7.3, 4.0	4.8	290	292.5	$205.3 \pm 97.0$	10.0	$13.9 \pm 9.6$	3.4
	P-2	5.4, 2.0	0.9	270	199.2		13.7		6.9
	P-3	5.1, 1.7	1.6	140	154.3		7.9		5.2
	P-4	6.4, 2.5	1.7	840	332.1		30.9		9.0
	P-5	6.8, 3.8	1.4	780	230.0		31.8		13.3
	P-6	7.8, 3.7	1.8	460	360.8		12.7		3.3
	P-7	7.0, 3.0	2.4	220	116.3		7.0		5.9
	P-8	6.7, 3.3	0.9	250	100.9		9.2		9.1
	P-9	9.5, 4.1	1.1	590	179.5		10.4		5.8
	P-10	9.5, 4.5	0.9	260	87.0		4.9		5.9
Pristine-G	P-G-1	6.1, 4.1	2.1	252	433.2	$221.9 \pm 86.9$	20.1	$17.4 \pm 7.0$	4.6
	P-G-2	8.5, 4.5	0.8	259	180.9		12.5		6.0
	P-G-3	7.2, 4.5	0.7	412	212.0		16.3		7.9
	P-G-4	7.7, 4.6	2.5	375	239.2		17.8		6.7
	P-G-5	8.3, 3.4	2.2	295	140.5		17.3		11.9
	P-G-6	7.7, 3.5	1.0	321	135.1		9.3		6.3
	P-G-7	8.6, 4.0	1.5	285	162.8		9.0		5.4
	P-G-8	8.7, 4.4	1.7	476	278.1		31.1		10.2
	P-G-9	9.3, 4.0	0.4	488	234.2		25.9		10.1
	P-G-10	7.3, 3.5	1.6	385	203.3		14.3		7.2
700PyC	C-1	9.4, 3.9	1.4	808	295.1	$201.8 \pm 100.9$	14.1	$10.2 \pm 4.3$	4.3
	C-2	10.1, 4.0	0.6	574	117.0		8.5		6.6
	C-3	7.7, 3.4	0.3	388	92.7		5.6		6.2
	C-4	8.0, 3.7	0.7	558	189.5		7.4		4.7
	C-5	7.9, 3.5	1.7	550	314.7		15.4		3.8
700PyC-G	C-G-1	10.5, 4.4	1.3	715	254.8	$294.9 \pm 100.0$	10.7	$18.7 \pm 6.2$	4.6
	C-G-2	9.6, 2.4	1.6	466	336.2		28.8		8.7
	C-G-3	9.7, 4.1	1.5	585	435.1		20.5		5.1
	C-G-4	8.0, 2.7	1.7	293	411.8		22.2		5.7
	C-G-5	9.0, 3.2	0.8	483	196.5		11.2		5.7
	C-G-6	9.6, 3.4	0.9	1299	270.3		20.8		7.8
	C-G-7	9.1, 4.8	2.1	940	373.4		20.2		5.3
	C-G-8	8.8, 4.1	1.4	480	156.6		10.1		6.7
	C-G-9	11.0, 3.6	0.7	485	344.0		24.0		7.4
	C-G-10	8.0, 2.2	0.4	852	170.6		18.8		11.8

vacancy recombination); however, the subsequent graphitization step may remove some  $sp^3$ -bonded atoms between CNT walls. Interestingly, the existence of the “clean break” in 700PyC-G samples implies that some interwall bonds (e.g.,  $sp^2$ - $sp^3$  cross-links) may remain in the two-step annealed CNTs.

The nominal strength of CNTs based on their whole cross-sectional area may be important for the design of CNT reinforced composites, which is affected by the fracture strength and the CNT

fracture behavior (interwall load transfer) [30]. From Table S4, 700PyC-G-CNTs exhibit a higher nominal strength and nominal modulus ( $10.4 \pm 4.6$  GPa,  $161.6 \pm 64.0$  GPa) compared to Pristine-G-CNTs ( $8.3 \pm 2.2$  GPa,  $111.1 \pm 43.6$  GPa). However, the nominal strength and modulus of 700PyC-G-CNTs are still comparable to those of Pristine-CNTs ( $10.8 \pm 7.3$  GPa,  $161.5 \pm 75.4$  GPa), probably because most 700C-G-CNTs exhibit the “sword-in-sheath” fracture rather than the “clean break.” The nominal

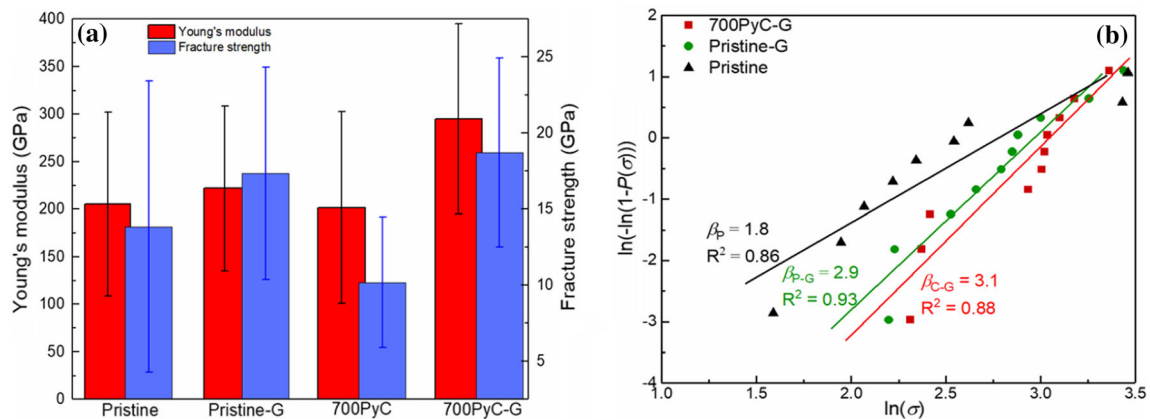
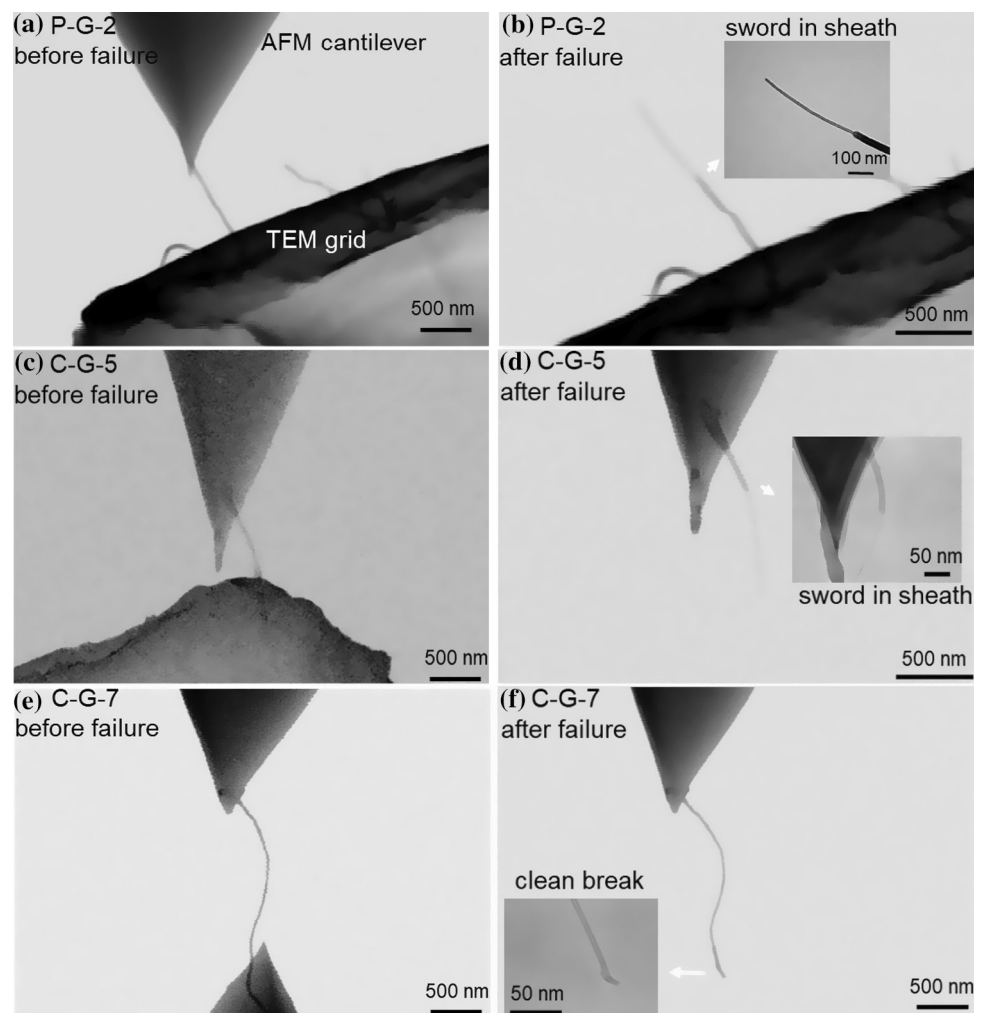


**Figure 4** Fracture strength and Young's modulus of Pristine-, Pristine-G-, 700PyC-, 700PyC-G-CNTs (a); the two-parameter Weibull strength distribution of Pristine-, Pristine-G-, 700PyC-G-

CNTs (b). The Weibull analysis has not included 700PyC-CNTs due to insufficient data points.

**Figure 5** SEM pictures of Pristine-G-CNTs before tension (a) and after tensile failure (b); SEM pictures of 700PyC-G-CNTs before tension (c, e) and after tensile failure (d, f), the inset in (b, d, f) shows the fractured morphology of CNTs obtained by TEM.



strength of two-step annealed CNTs is expected to be further improved after forming more interwall cross-links, e.g., by increasing the carbon supplying time

during the pyrolysis step or by adjusting the annealing temperature during the graphitization step.

For nanographite-based materials including CNTs, the Raman D/G intensity ratio can evaluate the in-plane crystallite size ( $L_a^R$ ) of a finite graphitic crystal. This universal method was initiated by Tuinstra and Koenig [55] for a calculation of graphene domain sizes. Here we suggest that the physical concept of  $L_a^R$  can be extended to the length of defect-free lattice fringes in CNTs (characteristic coherence length) [56], which actually reflects the size of homogenous vibrational domains [57]. In other words,  $L_a^R$  can estimate the average separation distance between significant structural defects (e.g., kinks, voids, flaws) along the nanotube length [37], so the linear defect density along the CNT length should be proportional to  $1/L_a^R$ . The semilogarithmic fitted line between  $\sigma$  and  $L_a^R$  is shown in Fig. S7a. It is reasonable that the fracture strength generally improves with an enlarged  $L_a^R$ , indicating that a smaller linear defect density along the CNT walls can contribute to the higher  $\sigma$ . Some numerical simulations [58, 59] have shown that the existence of kinks or discontinuous flaws along the CNT walls may induce the stress concentration and the resulting fracture. The fitted line between Young's modulus and  $L_a^R$  is shown in Fig. S7b. The general trend between the two has been approximated by a linear relationship. Indeed, the higher Young's modulus can be ascribed to the lower disorder degree (larger  $L_a^R$ ) in the CNT microstructure. Moreover, the experimental values of  $L_a^R$  shown in Table 1 are observed to have some correspondence with the  $L_a$  and  $L_c$  from XRD, and the  $\theta$  from FFT analysis. Thus, we used the  $L_a^R$  as a representative parameter with regard to the degree of defect densities to characterize the nanostructure of the CNTs tested in this study.

As shown above, two-step annealed CNTs (700PyC-G) show the increased in-plane crystallite size ( $L_a^R$ ) compared to one-step annealed CNTs (Pristine-G). Also, 700PyC-G-CNTs with the lower density of structural defects exhibit the improved tensile properties compared to Pristine-G-CNTs. It can be explained by straightening CNT walls and merging discontinuous graphene domains, which is facilitated by epitaxial PyC layers as the carbon supplying source during the high-temperature graphitization step. Therefore, we have developed the two-step annealed CVD-grown CNTs with a high crystallinity and good mechanical properties (especially the Young's modulus), which may have a potential application in nanoscale electronic devices

such as carbon nanotube tips for atomic force microscopy [60].

## Conclusions

In this study, by examining the microstructure and tensile properties of annealed CVD-grown CNTs, we find that the defect healing effect of two-step annealed CNTs (700PyC-G) is more desirable than that of one-step annealed CNTs (Pristine-G), which is resulted from their different structural evolution processes. In situ tensile tests indicate that the average Young's modulus and fracture strength of two-step annealed CNTs are better than those of one-step annealed CNTs, improved approximately by 35% and 10%, respectively. The in-plane crystallite size  $L_a^R$  calculated from Raman spectra can be used to reflect the linear defect density of CNTs, and the data fitting between tensile properties and  $L_a^R$  suggests that the CNT strength and Young's modulus are strongly dependent on the defect density along the nanotube length. Our results provide a fundamental study toward the structural annealing of CVD-grown CNTs, which may contribute to the tensile property improvement of CNTs and overcome the CNT property limit imposed by structural defects.

## Acknowledgements

The authors thank Dr. T Miyazaki from the Technical Division, School of Engineering, Tohoku University, for technical assistance in TEM analysis; we thank Professors T Wada and H Kato from the Institute for Materials Research, Tohoku University, for their helpful suggestions; we thank Dr. K Takahashi from Toyota ZEV Factory for the technical assistance; we thank LINTEC OF AMERICA, INC., Nano-Science & Technology Center (NSTC), for supplying the MWCNT sheets. This work was supported by JSPS KAKENHI Grant Number JP19K14837.

## Author Contributions

FL had contributed to conceptualization and methodology, and wrote the original draft; FL and TH carried out structure analysis; KS and TH were involved in writing, reviewing and editing and

funding acquisition. All authors have read and agreed to the submitted version of the manuscript.

**Supplementary Information:** The online version contains supplementary material available at <http://doi.org/10.1007/s10853-021-06523-8>.

## References

- [1] Mielke SL, Belytschko T, Schatz GC (2007) Nanoscale fracture mechanics. *Annu Rev Phys Chem* 58:185–209. <https://doi.org/10.1146/annurev.physchem.58.032806.104502>
- [2] Inoue Y, Hayashi K, Karita M et al (2021) Study on the mechanical and electrical properties of twisted CNT yarns fabricated from CNTs with various diameters. *Carbon* 176:400–410. <https://doi.org/10.1016/j.carbon.2021.01.139>
- [3] Shimamura Y, Oshima K, Tohgo K et al (2014) Tensile mechanical properties of carbon nanotube/epoxy composite fabricated by pultrusion of carbon nanotube spun yarn preform. *Compos Part A Appl Sci Manuf* 62:32–38. <https://doi.org/10.1016/j.compositesa.2014.03.011>
- [4] Kumar M, Ando Y (2010) Chemical vapor deposition of carbon nanotubes: a review on growth mechanism and mass production. *J Nanosci Nanotechnol* 10:3739–3758. <https://doi.org/10.1166/jnn.2010.2939>
- [5] Lukić B, Seo JW, Couteau E et al (2005) Elastic modulus of multi-walled carbon nanotubes produced by catalytic chemical vapour deposition. *Appl Phys A* 80:695–700. <https://doi.org/10.1007/s00339-004-3100-5>
- [6] Yamamoto G, Suk JW, An J et al (2010) The influence of nanoscale defects on the fracture of multi-walled carbon nanotubes under tensile loading. *Diam Relat Mater* 19:748–751. <https://doi.org/10.1016/j.diamond.2010.01.045>
- [7] Shirasu K, Kitayama S, Liu F et al (2021) Molecular dynamics simulations and theoretical model for engineering tensile properties of single- and multi-walled carbon nanotubes. *Nanomaterials* 11:795. <https://doi.org/10.3390/nano11030795>
- [8] Chiang WH, Futaba DN, Yumura M, Hata K (2011) Growth control of single-walled, double-walled, and triple-walled carbon nanotube forests by a priori electrical resistance measurement of catalyst films. *Carbon* 49:4368–4375. <https://doi.org/10.1016/j.carbon.2011.06.015>
- [9] Hou PX, Liu C, Cheng HM (2008) Purification of carbon nanotubes. *Carbon* 46:2003–2025. <https://doi.org/10.1016/j.carbon.2008.09.009>
- [10] Shirasu K, Tamaki I, Miyazaki T et al (2017) Key factors limiting carbon nanotube strength: structural characterization and mechanical properties of multi-walled carbon nanotubes. *Mech Eng J* 4:17–00029. <https://doi.org/10.1299/mej.17-00029>
- [11] Hansson J, Nylander A, Flygare M et al (2020) Effects of high temperature treatment of carbon nanotube arrays on graphite: increased crystallinity, anchoring and inter-tube bonding. *Nanotechnology* 31:455708. <https://doi.org/10.1088/1361-6528/ab9677>
- [12] Chen J, Shan JY, Tsukada T et al (2007) The structural evolution of thin multi-walled carbon nanotubes during isothermal annealing. *Carbon* 45:274–280. <https://doi.org/10.1016/j.carbon.2006.09.028>
- [13] Kim YA, Hayashi T, Osawa K et al (2003) Annealing effect on disordered multi-wall carbon nanotubes. *Chem Phys Lett* 380:319–324. <https://doi.org/10.1016/j.cplett.2003.09.027>
- [14] Andrews R, Jacques D, Qian D, Dickey EC (2001) Purification and structural annealing of multiwalled carbon nanotubes at graphitization temperatures. *Carbon* 39:1681–1687. [https://doi.org/10.1016/S0008-6223\(00\)00301-8](https://doi.org/10.1016/S0008-6223(00)00301-8)
- [15] Huang JY, Chen S, Jo SH et al (2005) Atomic-scale imaging of wall-by-wall breakdown and concurrent transport measurements in multiwall carbon nanotubes. *Phys Rev Lett* 94:236802. <https://doi.org/10.1103/PhysRevLett.94.236802>
- [16] Srikanth I, Padmavathi N, Prasad PSR et al (2016) Effect of high-temperature heat treatment duration on the purity and microstructure of MWCNTs. *Bull Mater Sci* 39:41–46. <https://doi.org/10.1007/s12034-015-0891-2>
- [17] Koshio A, Yudasaka M, Iijima S (2007) Disappearance of inner tubes and generation of double-wall carbon nanotubes from highly dense multiwall carbon nanotubes by heat treatment. *J Phys Chem C* 111:10–12. <https://doi.org/10.1021/jp0672914>
- [18] Zhang K, Malcolm Stocks G, Zhong J (2007) Melting and premelting of carbon nanotubes. *Nanotechnology* 18:285703. <https://doi.org/10.1088/0957-4484/18/28/285703>
- [19] Barber AH, Andrews R, Schadler LS, Wagner HD (2005) On the tensile strength distribution of multiwalled carbon nanotubes. *Appl Phys Lett* 87:1–3. <https://doi.org/10.1063/1.2130713>
- [20] Yamamoto G, Shirasu K, Nozaka Y et al (2014) Structure-property relationships in thermally-annealed multi-walled carbon nanotubes. *Carbon* 66:219–226. <https://doi.org/10.1016/j.carbon.2013.08.061>
- [21] Wei XL, Chen Q, Peng LM et al (2010) In situ measurements on individual thin carbon nanotubes using nanomanipulators inside a scanning electron microscope. *Ultramicroscopy* 110:182–189. <https://doi.org/10.1016/j.ultramic.2009.11.007>

- [22] Cheng Y, Li X, Gao H et al (2020) Diameter, strength and resistance tuning of double-walled carbon nanotubes in a transmission electron microscope. *Carbon* 160:98–106. <https://doi.org/10.1016/j.carbon.2020.01.012>
- [23] Peng B, Locascio M, Zapol P et al (2008) Measurements of near-ultimate strength for multiwalled carbon nanotubes and irradiation-induced crosslinking improvements. *Nat Nanotechnol* 3:626–631. <https://doi.org/10.1038/nnano.2008.211>
- [24] Salvétat JP, Kulik AJ, Bonard JM et al (1999) Elastic modulus of ordered and disordered multiwalled carbon nanotubes. *Adv Mater* 11:161–165. [https://doi.org/10.1002/\(SICI\)1521-4095\(199902\)11:2%3c161::AID-ADMA161%3e3.0.CO;2-J](https://doi.org/10.1002/(SICI)1521-4095(199902)11:2%3c161::AID-ADMA161%3e3.0.CO;2-J)
- [25] Ding W, Calabri L, Kohlhaas KM et al (2007) Modulus, fracture strength, and brittle vs. plastic response of the outer shell of arc-grown multi-walled carbon nanotubes. *Exp Mech* 47:25–36. <https://doi.org/10.1007/S11340-006-9344-6>
- [26] Yu MF, Lourie O, Dyer MJ et al (2000) Strength and breaking mechanism of multiwalled carbon nanotubes under tensile load. *Science* 287:637–640. <https://doi.org/10.1126/science.287.5453.637>
- [27] Demczyk BG, Wang YM, Cumings J et al (2002) Direct mechanical measurement of the tensile strength and elastic modulus of multiwalled carbon nanotubes. *Mater Sci Eng A* 334:173–178. [https://doi.org/10.1016/S0921-5093\(01\)01807-X](https://doi.org/10.1016/S0921-5093(01)01807-X)
- [28] Faraji S, Stano K, Rost C et al (2014) Structural annealing of carbon coated aligned multi-walled carbon nanotube sheets. *Carbon* 79:113–122. <https://doi.org/10.1016/j.carbon.2014.07.049>
- [29] Beese AM, Papkov D, Li S et al (2013) In situ transmission electron microscope tensile testing reveals structure-property relationships in carbon nanofibers. *Carbon* 60:246–253. <https://doi.org/10.1016/j.carbon.2013.04.018>
- [30] Shirasu K, Yamamoto G, Hashida T (2019) How do the mechanical properties of carbon nanotubes increase? An experimental evaluation and modeling of the engineering tensile strength of individual carbon nanotubes. *Mater Res Express* 6:055047. <https://doi.org/10.1088/2053-1591/ab069f>
- [31] Monthieux M, Allouche H, Jacobsen RL (2006) Chemical vapour deposition of pyrolytic carbon on carbon nanotubes. Part 3: Growth mechanisms. *Carbon* 44:3183–3194. <https://doi.org/10.1016/j.carbon.2006.07.001>
- [32] Krasnikov DV, Kuznetsov VL, Romanenko AI, Shmakov AN (2018) Side reaction in catalytic CVD growth of carbon nanotubes: surface pyrolysis of a hydrocarbon precursor with the formation of lateral carbon deposits. *Carbon* 139:105–117. <https://doi.org/10.1016/j.carbon.2018.06.033>
- [33] Elumeeva KV, Kuznetsov VL, Ischenko AV et al (2013) Reinforcement of CVD grown multi-walled carbon nanotubes by high temperature annealing. *AIP Adv* 3:112101. <https://doi.org/10.1063/1.4829272>
- [34] Muniz FTL, Miranda MAR, Morilla Dos Santos C, Sasaki JM (2016) The Scherrer equation and the dynamical theory of X-ray diffraction. *Acta Crystallogr Sect A Found Adv* 72:385–390. <https://doi.org/10.1107/S205327331600365X>
- [35] Pope CG (1997) X-ray diffraction and the bragg equation. *J Chem Educ* 74:129–131. <https://doi.org/10.1021/ed074p129>
- [36] Faraji S, Yildiz O, Rost C et al (2017) Radial growth of multi-walled carbon nanotubes in aligned sheets through cyclic carbon deposition and graphitization. *Carbon* 111:411–418. <https://doi.org/10.1016/j.carbon.2016.10.012>
- [37] Velasquez M, Batiot-Dupeyrat C, Gallego J, Santamaria A (2014) Chemical and morphological characterization of multi-walled-carbon nanotubes synthesized by carbon deposition from an ethanol-glycerol blend. *Diam Relat Mater* 50:38–48. <https://doi.org/10.1016/j.diamond.2014.08.015>
- [38] Capado LG, Takai K, Enoki T et al (2006) General equation for the determination of the crystallite size  $l_a$  of nanographite by Raman spectroscopy. *Appl Phys Lett* 88:163106. <https://doi.org/10.1063/1.2196057>
- [39] Kuznetsov VL, Bokova-Sirosh SN, Moseenkov SI et al (2014) Raman spectra for characterization of defective CVD multi-walled carbon nanotubes. *Phys status solidi* 251:2444–2450. <https://doi.org/10.1002/pssb.201451195>
- [40] Lehman JH, Terrones M, Mansfield E et al (2011) Evaluating the characteristics of multiwall carbon nanotubes. *Carbon* 49:2581–2602. <https://doi.org/10.1016/j.carbon.2011.03.028>
- [41] Shirasu K, Asaoka M, Miyazaki T et al (2019) Stack-coating of multishell carbon layers templated with carbon nanotubes. *Mater Today Commun* 21:100608. <https://doi.org/10.1016/j.mtcomm.2019.100608>
- [42] Ding F, Jiao K, Lin Y, Yakobson BI (2007) How evaporating carbon nanotubes retain their perfection? *Nano Lett* 7:681–684. <https://doi.org/10.1021/nl0627543>
- [43] Ding F, Jiao K, Wu M, Yakobson BI (2007) Pseudoclimb and dislocation dynamics in superplastic nanotubes. *Phys Rev Lett* 98:075503. <https://doi.org/10.1103/PhysRevLett.98.075503>
- [44] Huang JY, Chen S, Ren ZF et al (2006) Kink formation and motion in carbon nanotubes at high temperatures. *Phys Rev Lett* 97:075501. <https://doi.org/10.1103/PhysRevLett.97.075501>
- [45] Chen MW, Zhu YB, Xia J, Wu HA (2019) Molecular insights into the initial formation of pyrolytic carbon upon carbon fiber surface. *Carbon* 148:307–316. <https://doi.org/10.1016/j.carbon.2019.04.003>

- [46] Chen J, Shi T, Cai T et al (2013) Self healing of defected graphene. *Appl Phys Lett* 102:103107. <https://doi.org/10.1063/1.4795292>
- [47] Kuznetsov VL, Elumeeva KV, Ishchenko AV et al (2010) Multi-walled carbon nanotubes with ppm level of impurities. *Phys status solidi* 247:2695–2699. <https://doi.org/10.1002/pssb.201000211>
- [48] Hada M, Hasegawa T, Inoue H et al (2019) One-minute joule annealing enhances the thermoelectric properties of carbon nanotube yarns via the formation of graphene at the interface. *ACS Appl Energy Mater* 2:7700–7708. <https://doi.org/10.1021/acsaem.9b01736>
- [49] De Silva KKH, Huang HH, Joshi R, Yoshimura M (2020) Restoration of the graphitic structure by defect repair during the thermal reduction of graphene oxide. *Carbon* 166:74–90. <https://doi.org/10.1016/j.carbon.2020.05.015>
- [50] Botari T, Paupitz R, da Silva A, Autreto P, Galvao DS (2016) Graphene healing mechanisms: a theoretical investigation. *Carbon* 99:302–309. <https://doi.org/10.1016/j.carbon.2015.11.070>
- [51] Klein CA (2007) Characteristic tensile strength and Weibull shape parameter of carbon nanotubes. *J Appl Phys* 101:124909. <https://doi.org/10.1063/1.2749337>
- [52] Gao E, Lu W, Xu Z (2018) Strength loss of carbon nanotube fibers explained in a three-level hierarchical model. *Carbon* 138:134–142. <https://doi.org/10.1016/j.carbon.2018.05.052>
- [53] Xia ZH, Guduru PR, Curtin WA (2007) Enhancing mechanical properties of multiwall carbon nanotubes via  $sp^3$  interwall bridging. *Phys Rev Lett* 98:245501. <https://doi.org/10.1103/PhysRevLett.98.245501>
- [54] Santo Pietro D, Tang C, Chen C (2012) Enhancing interwall load transfer by vacancy defects in carbon nanotubes. *Appl Phys Lett* 100:033118. <https://doi.org/10.1063/1.3678342>
- [55] Tuinstra F, Koenig JL (1970) Raman spectrum of graphite. *J Chem Phys* 53:1126–1130. <https://doi.org/10.1063/1.1674108>
- [56] Delhaes P, Couzi M, Trinquecoste M et al (2006) A comparison between Raman spectroscopy and surface characterizations of multiwall carbon nanotubes. *Carbon* 44:3005–3013. <https://doi.org/10.1016/j.carbon.2006.05.021>
- [57] Osswald S, Havel M, Gogotsi Y (2007) Monitoring oxidation of multiwalled carbon nanotubes by Raman spectroscopy. *J Raman Spectrosc* 38:728–736. <https://doi.org/10.1002/jrs.1686>
- [58] Zhang S, Mielke SL, Khare R et al (2005) Mechanics of defects in carbon nanotubes: atomistic and multiscale simulations. *Phys Rev B - Condens Matter Mater Phys* 71:115403. <https://doi.org/10.1103/PhysRevB.71.115403>
- [59] Zhu L, Wang J, Ding F (2016) The great reduction of a carbon nanotube's mechanical performance by a few topological defects. *ACS Nano* 10:6410–6415. <https://doi.org/10.1021/acsnano.6b03231>
- [60] Wilson NR, Macpherson JV (2009) Carbon nanotube tips for atomic force microscopy. *Nat Nanotechnol* 4:483–491. <https://doi.org/10.1038/nnano.2009.154>

**Publisher's Note** Springer Nature remains neutral with regard to jurisdictional claims in published maps and institutional affiliations.